Lateral Electron Transport in High-Intensity Laser-Irradiated Foils Diagnosed by Ion Emission

P. McKenna,[1,2,*] D. C. Carroll,[1] R. J. Clarke,[2] R. G. Evans,[2,5] K. W. D. Ledingham,[1,†] F. Lindau,[3] O. Lundh,[3] T. McCanny,[1] D. Neely,[2] A. P. L. Robinson,[2] L. Robson,[1,†] P. T. Simpson,[4] C.-G. Wahlström,[3] and M. Zepf[4]

[1]*SUPA, Department of Physics, University of Strathclyde, Glasgow G4 0NG, United Kingdom*
[2]*CCLRC, Rutherford Appleton Laboratory, Chilton, Didcot, Oxon OX14 0QX, United Kingdom*
[3]*Department of Physics, Lund University, P.O. Box 118, S-22100 Lund, Sweden*
[4]*Department of Physics and Astronomy, Queen's University Belfast, Belfast BT7 1NN, United Kingdom*
[5]*Department of Physics, Imperial College, London, SW7 2AZ, United Kingdom*

(Received 16 December 2006; published 4 April 2007)

An experimental investigation of lateral electron transport in thin metallic foil targets irradiated by ultraintense ($\geq 10^{19}$ W/cm^2) laser pulses is reported. Two-dimensional spatially resolved ion emission measurements are used to quantify electric-field generation resulting from electron transport. The measurement of large electric fields ($\sim$0.1 TV/m) millimeters from the laser focus reveals that lateral energy transport continues long after the laser pulse has decayed. Numerical simulations confirm a very strong enhancement of electron density and electric field at the edges of the target.

DOI: 10.1103/PhysRevLett.98.145001 PACS numbers: 52.50.Jm, 41.75.Jv, 52.70.Nc

The study of fast electron generation and transport in intense laser interactions with dense plasma is of fundamental importance for the fast ignition approach to inertial fusion [1]. It is also important for the optimization of high power laser-driven ion [2–5] and x-ray sources [6]. One of the factors influencing the efficiency of longitudinal energy transport in a laser-irradiated target is the degree of lateral spreading of the energetic electron population. In the 1980s experimental and theoretical investigations, at laser intensities up to $\sim 10^{16}$ W/cm^2, revealed that of the order of 30% of the absorbed laser energy is transported laterally by energetic electrons [7–9]. Recently there has been significant interest in electron transport along the surface of targets irradiated by ultraintense ($>10^{18}$ W/cm^2) laser pulses [10–12], in relation to the physics of cone guided schemes for fast ignition [13].

In this Letter we present an experimental investigation of lateral electron transport in ultraintense laser-irradiated foils, diagnosed via spatially resolved measurements of multi-MeV ion emission. The principal diagnostics used in experimental investigations of electron transport in solid targets typically involve, for example, measurement of $K\alpha$ emission from buried layers [14,15]. Ion emission has previously been used to investigate electron energy transport through a solid target [16] and field dynamics at the rear of a target foil, opposite to the laser focal spot [17,18]. Here we observe and measure ion emission from the edges of thin target foils, where the edges are sufficiently far away from the focal spot that the expanding electron cloud cannot reach them until a long time after the laser pulse. We use this ion emission to make quantitative measurements of the 2D spatial distribution of electric-field (E-field) formation due to lateral electron transport in the foil. Our experimental measurements and simulations using the LSP code [an implicit particle-in-cell (PIC) model with fluid background] [19] reveal enhanced electron densities and E fields at solid-vacuum boundaries, and shed light on the dynamics of the expansion of the electron cloud.

The experiment used the Vulcan laser at the Rutherford Appleton Laboratory, UK. Pulses of wavelength 1.053 μm, energy up to 400 J and duration 1 ps (FWHM) are focused using an $f/3$ off-axis parabola to intensities up to 6×10^{20} W/cm^2. The level of the amplified spontaneous emission (ASE) is measured to be 10^{-7} and 10^{-6} of the peak laser intensity at a few nanoseconds and a few picoseconds prior to the peak of the pulse, respectively. The pulses are p polarized and incident onto target at 45°. A schematic of the experiment arrangement is shown in Fig. 1(a).

The targets are 10 μm thick planar Au and Al foils of size 4 mm $\times$ 10 mm. Foils with 50 μm diameter "witness" holes machined 500 μm from the laser focus are also used. The Au targets are resistively heated to 1000 °C for 10 min prior to and during laser irradiation to reduce the hydrogenated contamination on the target surfaces.

The charge-to-mass ratio and energy of ions emitted from the target are measured using a high-resolution Thomson spectrometer incorporating a 0.6 T, 50 mm long magnetic field, and an electric field which varies in strength from 3.0 to 0.3 kV/mm over a distance of 200 mm. The solid angle is varied between 5×10^{-9} and 2×10^{-7} sr, depending on the ion flux. Ions (and fast neutral atoms) are detected using CR-39 plastic track detectors positioned in the dispersion plane of the spectrometer. CR-39 is sensitive to ions, but insensitive to electrons and electromagnetic radiation. Each ion entering the CR-39 damages the plastic and a corresponding "pit" (between 5 and 20 μm diameter) is produced after etching in NaOH solution. The spatial distribution of the pits is mapped out using an automated scanning microscope with pit recognition and analysis software [20]. Ions of a given

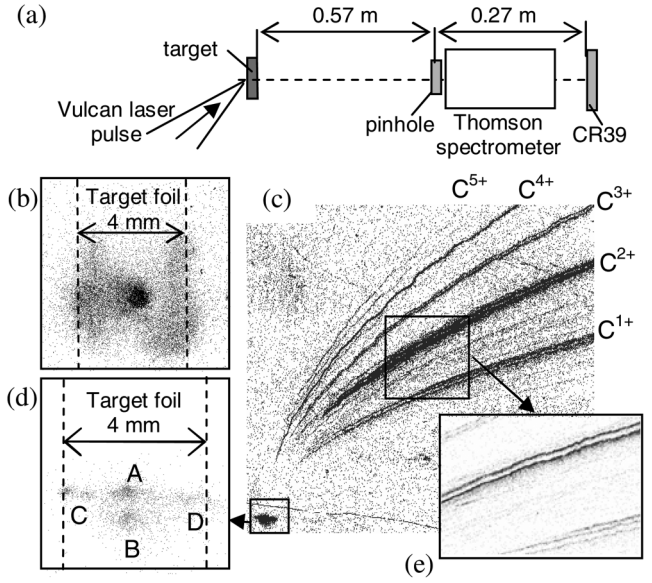

FIG. 1. (a) Schematic of the experiment arrangement in which a Thomson spectrometer is used as an ion pinhole camera. (b) Optical scanned image of pits in CR-39 produced by fast uncharged atoms (recombined ions). Ions are accelerated from a central spot and from linear regions corresponding to the target edge. (c) Spatial mapping of pit distributions on a CR-39 detector in the dispersion plane of a Thomson spectrometer, produced using an automated scanning microscope with pit recognition software [20]. Mainly carbon ions are detected in distinct ion traces. (d) Enlarged region corresponding to fast neutral atoms undeflected in the spectrometer fields. Source regions are observed at the center of the target foil, A, at the edge of a 50 μm hole, B, and at the edges of the foil, C and D. (e) Enlarged region showing multiple carbon ion tracks. Each track results from one of the four source regions in (d).

charge-to-mass ratio originating from a point source produce a single signature parabolic track of pits in the CR-39. The coordinates of every pit in a given track are extracted to determine the ion energy spectrum.

In good agreement with previous results we find that protons are the dominant ions emitted in laser interactions with unheated targets, and that carbon ions are efficiently accelerated when target foils are heated [17,21]. However, unexpectedly we observe ions from more than one source region on the target foil. In particular, we find that, regardless of whether we irradiate Al or Au foils, heated or unheated, we observe ion emission from the edges of the target foils, 2 mm on either side of the laser focal spot.

To illustrate the observation Fig. 1(b) shows part of an optically scanned image of pits produced in a CR-39 sample. The Thomson spectrometer in this example was positioned along target normal and at the rear of a 10 μm thick unheated Al target irradiated by a 200 J, 1 ps, 3×10^{20} W/cm^2 laser pulse. The image is produced by fast neutral atoms, which are observed on every shot and result from fast ions undergoing recombination before entering the spectrometer. The pits produced by these recombined ions mark the zero-deflection axis of the spectrometer onto the CR-39 detector. The 300 μm diameter aperture at the entrance to the spectrometer in combination with the spatially resolving detection facilitated by the CR-39 effectively works as a demagnifying pinhole camera of fast-ion emission from the target. Figure 1(b) is therefore a 2D spatially resolved measurement of ion emission. The magnification factor is 0.47 and the spatial resolution, which is a function of the aperture size, is 930 μm for the measurement in Fig. 1(b). Most ions are emitted from a central spot on the target, opposite to the laser focal spot on the front surface. Linear regions of ion emission on either side of the central spot are clearly observed, and the demagnification factor confirms that these ions are emitted from the edges of the target, 2 mm on either side of the focal spot.

Next we investigate the ion species accelerated from each of the source regions by increasing the spatial resolution of the spectrometer to 155 μm and looking for multiple sets of ion tracks on the CR-39 detector. Figure 1(c) shows a spatial mapping, at the higher resolution, of pits distributed in a full CR-39 detector. This particular measurement was obtained with a 340 J energy laser pulse focused to a spot size of 40 μm (FWHM), corresponding to an intensity of 1×10^{19} W/cm^2, onto a heated Au foil target. The main tracks are produced by C ions from hydrocarbon contamination layers. Two main features of interest in the figure are enlarged. The first is the signal produced by the recombined ions, Fig. 1(d). As before, we observe ion emission from the edges of the target (C and D). The signal is considerably reduced compared to the result shown in Fig. 1(b) due to a factor of 36 reduction in the solid angle sampled by the spectrometer and a factor 30 reduction in laser intensity. Another ion source (B), vertically offset from the main source (A), corresponds to emission from the edge of a 50 μm diameter witness hole positioned 500 μm from the focal spot. The total recombined ion signal from the four sources is $\sim$3% of the total ion signal detected on the CR-39, in good agreement with previous estimates for experiments of this type [17]. Importantly, with the higher spatial resolution we observe multiple ion tracks for many of the charge states of carbon, as shown in Fig. 1(e). Each track has been identified as resulting from one of the four ion sources shown in Fig. 1(d), revealing that, in addition to the main source (A) carbon ions are also emitted from the edges of the irradiated target foil and the hole, as listed in Table I.

We use carbon ion emission to diagnose E-field generation using the method described by Hegelich *et al.* [17] and used by Schreiber *et al.* [18]. The charge states observed provide a measure of the peak E-field strength and the ion energy spectra provides information on the temporal and spatial extent of the field. Because of the stopping range of multi-MeV C ions in Au, we assume that the energetic C ions detected originate on the rear surface of the target. We rule out ionization at the rear of the target as arising due to

TABLE I. C^{q+} ions observed from each of the four sources (A–D) in Fig. 1 and calculated field parameters. E_q^{thresh} is the lower threshold E field required to produce a carbon ion of charge q. $E_q^{\max}$ is the maximum E field and is used to calculate $\tau_q^{\min}$ and $l_q^{\min}$, the minimum field duration and acceleration length, respectively, to accelerate the ionic charge state to the detected maximum energy $W_q^{\max}$.

	q	$W_q^{\max}$ (MeV)	E_q^{thresh} (TV/m)	$E_q^{\max}$ (TV/m)	$\tau_q^{\min}$ (ps)	$l_q^{\min}$ (μm)
A	1	3.4	0.022	0.052	18	67
	2	5.4	0.052	0.13	4.4	21
	3	11	0.13	0.18	3.1	21
	4	25	0.18	5.3	0.12	1.2
	5	38	5.3	7.0	0.09	1.1
B	1	4.7	0.022	0.052	21	92
	2	5.9	0.052	0.13	4.6	22
	3	19	0.13	0.18	4.0	35
C	1	1.5	0.022	0.052	12	30
	2	4.4	0.052	0.13	4.0	17
D	2	...	0.052	0.13	...	...

the laser pulse, as it is absorbed in the preplasma, or due to a shock wave driven by the ASE, due to the thickness and density of the target foil. Similar to Hegelich *et al.* [17] we calculate the collisional ionization rate due to the hot electrons and the cold electron return current and find it to be lower than the ionization rate due to field ionization by barrier suppression (FIBS) for C^{q+}: $q = 1$–4, and thereby assume FIBS to be the dominant ionization mechanism at the rear of the target. The threshold field E_q^{thresh} for the production of each ion of charge q is calculated using

$$E_q^{\text{thresh}} = U_{q-1}^2 \varepsilon_0 \pi / qe, \tag{1}$$

where U_q is the ionization potential in eV. A lower limit for the acceleration time τ and the acceleration length l (minimum longitudinal spatial extent of the field) required to produce the measured maximum energy of each ion species from each source is calculated assuming that a given ion of charge q will experience a maximum electric-field strength given by $E_q^{\max} = E_{q+1}^{\text{thresh}}$, the threshold for further ionization. The calculated parameters for each of the four sources are presented in Table I.

We find that the highest field strength, >5.3 TV/m, is produced in the region of the target rear surface opposite to the laser focal spot. A field of between 0.13 and 0.18 TV/m is generated on the edge of the hole 0.5 mm from the focal spot and fields of between 0.05 and 0.13 TV/m are generated at the target edges. E fields of this order 2 mm away from the focal spot indicate that the lateral transport of energetic electrons in the foil continues long after the laser pulse. This is consistent with time resolved measurements of $K\alpha$ x-ray production for thin, isolated targets [22].

To demonstrate that this picture of the expanding charge cloud is realistic we perform 2D cylindrical simulations of the charge cloud dynamics with the LSP computer model [19] using a kinetic (PIC) description of the energetic electrons and a fluid description of the bulk of the target. The simulation grid covers 600 μm $\times$ 600 μm with 2400×2400 cells. The cell size of 0.25 μm is just adequate to resolve the distribution of electrons in the bulk of the 10 μm thick target foils, but does not enable investigation of ion dynamics. Electrons are created to correspond to the distribution of accelerated electrons from the laser. A laser-to-electron energy conversion efficiency of 30% is assumed and the mean electron energy is 1 MeV, equal to the ponderomotive potential, for a laser intensity of 10^{19} W/cm^2.

For a laser pulse of duration T the electron temperature is increased over $0.1T$, held constant for $0.8T$, and decreased over $0.1T$. The axial distribution corresponds to half of a relativistic thermal distribution (in the laser direction) and the angular spread is around 30° half-angle. Most of the electrons pass through the target and are reflected in the expanding Debye sheath on the rear surface. The motion of the Debye sheath results in a reduction of the axial component of electron velocity while the transverse velocity is largely unaltered. As the electrons reflux [23] within the foil many times the charge cloud expands out laterally forming a disk. The radial expansion requires a return current to flow via the "cold" electrons of the target foil, and the resistivity of the target gives rise to an E field which hinders the expansion. Because of the fall off in current density as the cloud expands radially, the effect of this E field rapidly diminishes with radius.

Our LSP simulations show a very strong enhancement of the electron density and E field when the charge cloud reaches the edge of the target disk, as illustrated in Fig. 2, where (a) and (b) show the hot electron density and magnitude of the resulting E field, respectively, after 0.25 ps; Figs. 1(c) and 1(d) show the corresponding results after 2.5 ps. At the edge of the target the return current is no longer supported and the expansion is halted by the radial component of the electrostatic field caused by the buildup of net negative charge. The electrons "pile up" at the target edge and are eventually reflected after a time of the order of the plasma period (350 fs for an electron density of 10^{17} cm^{-3}). The E fields at the target edge in the simulation (400 μm radius) are about 0.2 TV/m and fields greater than 0.02 TV/m extend out to a distance of about 15 μm from the target.

Figure 2(e) shows how the temporal evolution of the E field (potential drop over a distance of 25 μm from the surface of the target in the direction normal to the surface) varies as a function of time for selected distances from the laser focal spot. As the simulation grid is smaller than the

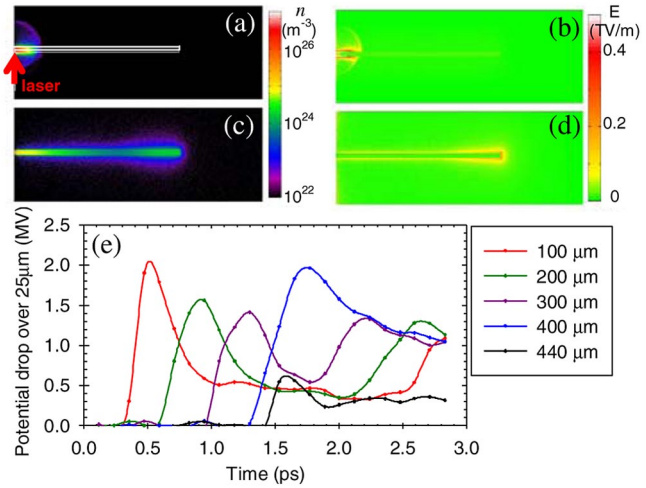

FIG. 2 (color online). (a) Electron density n 0.25 ps after the start of the laser pulse. The target profile (400 μm radius and 10 μm thickness) is illustrated by the white line. The simulation space is cylindrically symmetric about the laser axis, marked by the (red) arrow. (b) Resultant E-field strength after 0.25 ps. (c),(d) Corresponding results 2.5 ps after the start of the laser pulse. (e) Temporal evolution of the potential drop over 25 μm from the surface of the target at given radii from the laser focal spot. The field becomes higher and remains high at the edge of the target (400 μm) for much longer than at smaller radii. A second later peak in the transient field at the smaller radii is produced by electrons which are reflected from the target edge and transverse the target again, in the opposite direction.

size of the target (the radius of the target in the simulation is 400 μm and in the experiment is 2 mm) the pulse duration in the simulation is 200 fs—scaled down to the transit time for the expanding charge cloud to reach the target edge. It is observed that the charge wave moves laterally at approximately $0.75c$ (where c is the speed of light in vacuum). The magnitude of the field at the edge remains large over a much longer duration than the transient field at other radii within the target. Although we see some ion emission across the target in our experiment, we predominantly observe ions from the laser focal spot and the target edges, indicating that ion emission as a diagnostic of E-field generation is more sensitive to the longer duration field at the edges. In this respect ion emission provides a unique probe of transient E-field strength in intense laser-foil interactions.

We have shown that there is significant lateral expansion of the electron cloud in thin foils irradiated by ultraintense laser pulses and that the electron motion is inhibited at target-vacuum interfaces, leading to the formation of strong electric fields and resulting in ionization and ion acceleration. Using ion emission to quantify the E field at varying distances from the laser focus, we have also shown that hot electron transport occurs long after the time of the laser pulse driver.

Two-dimensional spatial mapping of ion emission complements other methods of E-field measurement such as proton probing [24], which provide an integrated measurement across the target surface, and opens the possibility to access new physics on transient E-field detection.

The authors would like to acknowledge the scientific and technical expertise of the personnel at the Vulcan Laser Facility. O. L. and F. L. acknowledge support from the COST program. M. Z. received support from the Royal Society.

*Author to whom correspondence should be addressed. Email address: p.mckenna@phys.strath.ac.uk
†Also at AWE plc, Aldermaston, Reading, RG7 4PR, UK.

[1] M. Tabak *et al.*, Phys. Plasmas **1**, 1626 (1994).
[2] S. C. Wilks *et al.*, Phys. Plasmas **8**, 542 (2001).
[3] M. Roth *et al.*, Phys. Rev. ST Accel. Beams **5**, 061301 (2002).
[4] P. Gibbon, Phys. Rev. E **72**, 026411 (2005).
[5] L. Robson *et al.*, Nature Phys. **3**, 58 (2007).
[6] C. Reich *et al.*, Phys. Rev. Lett. **84**, 4846 (2000).
[7] K. Eidmann *et al.*, Appl. Phys. Lett. **43**, 440 (1983).
[8] D. W. Forslund and J. U. Brackbill, Phys. Rev. Lett. **48**, 1614 (1982).
[9] F. Amiranoff *et al.*, J. Phys. D **15**, 2463 (1982).
[10] T. Nakamura *et al.*, Phys. Rev. Lett. **93**, 265002 (2004).
[11] Y. T. Li *et al.*, Phys. Rev. Lett. **96**, 165003 (2006).
[12] H. Habara *et al.*, Phys. Rev. Lett. **97**, 095004 (2006).
[13] Y. Sentoku *et al.*, Phys. Plasmas **11**, 3083 (2004).
[14] S. D. Baton *et al.*, Plasma Phys. Controlled Fusion **47**, B777 (2005).
[15] P. K. Patel *et al.*, Plasma Phys. Controlled Fusion **47**, B833 (2005).
[16] G. D. Tsakiris *et al.*, Phys. Rev. Lett. **46**, 1202 (1981).
[17] M. Hegelich *et al.*, Phys. Rev. Lett. **89**, 085002 (2002).
[18] J. Schreiber *et al.*, Appl. Phys. B **79**, 1041 (2004).
[19] D. R. Welch *et al.*, Nucl. Instrum. Methods Phys. Res., Sect. A **464**, 134 (2001).
[20] TASL-IMAGE, Track Analysis Systems Limited. Details online at www.tasl.co.uk.
[21] P. McKenna *et al.*, Phys. Rev. E **70**, 036405 (2004).
[22] J. C. Kieffer *et al.*, J. Opt. Soc. Am. B **13**, 132 (1996).
[23] Y. Sentoku *et al.*, Phys. Plasmas **10**, 2009 (2003).
[24] M. Borghesi *et al.*, Phys. Plasmas **9**, 2214 (2002).